Dual-mechanism transition controls rupture development of large deep earthquakes

Zhe Jia[1,2*], Wenyuan Fan[2], Wei Mao[3], Peter Shearer[2], Dave A. May[2]

[1]Institute for Geophysics, Jackson School of Geosciences, UT Austin, Austin, Texas, USA
[2]Scripps Institution of Oceanography, UC San Diego, La Jolla, California, USA
[3]Seismological Laboratory, California Institute of Technology, Pasadena, California, USA

[*]Corresponding author; E-mail: zjia@ig.utexas.edu

Short title: Mechanism transition controls deep earthquakes

Teaser: Shift from mineral transition to rock melting explains deep earthquake rupture characteristics at global subduction zones

Abstract

Deep earthquakes at depths below 500 km are under prohibitive pressure and temperature conditions for brittle failure. Individual events show diverse rupture behaviors, and a coherent mechanism to explain their rupture nucleation, propagation, and characteristics has yet to be established. We systematically resolve the rupture processes of 40 large $M > 7$ deep earthquakes from 1990–2023 and compare the rupture details to their local metastable olivine wedge (MOW) structures informed from thermo-mechanical simulations in seven subduction zones. Our results suggest that these events likely initiate from metastable olivine transformations within the cold slab core and rupture be-

yond the MOW due to sustained weakening from molten rock at the rupture tip. Over half of the $M > 7$ earthquakes likely rupture beyond the MOW boundary and are controlled by both mechanisms. Rupturing outside the MOW boundary leads to greater moment release, increased geometric complexity, and a reduction in rupture length, causing greater stress drops.

Introduction

Deep earthquakes occurring at depths between 500 and 700 km challenge our understanding of earthquake physics. At these depths, the extreme confining pressure and high temperature are prohibitive for brittle failure and frictional sliding, which drive typical shallow earthquakes (*1, 2*). However, earthquakes with magnitudes (M) greater than 7 occur at these depths almost every year (*3*). These deep seismic events share similar source characteristics to crustal earthquakes, such as double-couple focal mechanisms and a Gutenberg-Richter magnitude-frequency distribution (*4, 5*). Deep earthquakes occur exclusively at subduction zones, and knowing their physical mechanisms can provide unique constraints on the geometry, structure, and dynamics of subducting slabs and the surrounding mantle structure near the 660-km discontinuity (*6–9*). Multiple competing mechanisms have been proposed to explain deep earthquake occurrence. However, a coherent mechanism that can explain the diversity of deep event properties has yet to be identified.

Observations of the rupture propagation and spatial extent of deep earthquakes provide constraints on their governing mechanisms. For example, the early stages of the 1994 Fiji M_W 7.5 and the 2013 Okhotsk M_W 8.3 deep earthquakes appear to rupture in similar ways to shallow earthquakes, with rupture lengths comparable to those of cold slab cores, yielding low stress drops during their initial ruptures (*10–13*). These rupture characteristics can be explained by the transformational faulting mechanism, which involves a phase transition of metastable olivine to wadsleyite or ringwoodite in the transition zone (depths of approximately 410 to 660 km) within the highly-stressed, cold slab cores. This phase transition can create a weak zone and trigger shear faulting, leading to earthquake nucleation and rupture propagation (*14–16*). Importantly, this phase transition is controlled by temperature (*17, 18*), and its temperature dependence defines a metastable olivine wedge (MOW). A MOW has been directly imaged in the Japan subducting slab (*19, 20*). Additionally, laboratory experiments on olivine at realistic pressure and temperature conditions have successfully reproduced transformational faulting and rupture nucleation (*21, 22*). However, the transformational faulting mechanism alone cannot fully explain all deep earthquakes. For example, the likely extent of MOWs is insufficient to accommodate the large ruptures of the 1994 Fiji and the 2013 Okhotsk events, suggesting additional processes that facilitate large earthquake rupture propagation (*23, 24*).

The thermal runaway mechanism is another process that can drive deep earthquakes (*1, 2*). This mechanism involves localized shear heating that weakens the rock, producing a molten shear band that lubricates the fault and sustains rupture propagation (*25, 26*). The thermal runaway mechanism is distinct from transformational faulting in that the latter involves shear dislocation along phase-transition generated weak zones, while the former results from localized heating that alters the frictional behavior of the fault. The thermal runaway mechanism has been used to explain some large deep earthquakes, such as the 1994 Bolivia M_W 8.2 earthquake. This event occurred in the warm South American slab, which had a limited supply of metastable olivine at the event depth, thus excluding the possibility of a pure transformational faulting mechanism driving the earthquake (*27, 28*). The Bolivia event likely ruptured a compact area and had a particularly high stress drop (*29, 30*), leading to the dissipation of most of its strain energy near the source (*31*), which may have triggered a shear thermal instability. However, shear thermal runaway alone cannot explain all deep earthquakes. For example, the 2018 Tonga-Fiji Mw 8.2 earthquake originated within the slab core and ruptured in two stages, each showing distinct characteristics in extent and high-frequency radiation (*32, 33*). These variations highlight the complexity of deep earthquakes.

Here, we conduct a comprehensive analysis of rupture processes for all large, deep earthquakes worldwide ($M > 7.0$) from 1990 to 2023. We derive subevent models to constrain the rupture propagations and dimensions of 40 deep events. By performing the same analysis for these events, we can identify statistically significant rupture variations to infer their driving mechanisms. Additionally, we model the local MOW structure across 31 profiles at seven subduction zones to examine the influence of the phase transformation mechanism on the rupture characteristics of deep earthquakes. Our results indicate that larger deep earthquakes often rupture beyond the confines of the MOWs. We find that, with increasing magnitude, deep earthquakes have larger stress drops and increased complexity in fault geometry and slip orientation. Collectively, these observations suggest a transition in rupture mechanism as earthquake moment increases, shifting from transformational faulting to shear thermal runaway. This mechanism transition is primarily determined by the ratio of the MOW width to the rupture extent. Our proposed mechanism transition connects two seemingly contradictory hypotheses and provides a coherent explanation for the varying rupture characteristics of large deep earthquakes.

Results

Rupture processes of global $M_w > 7$ deep earthquakes

We image the rupture processes and dimensions of 40 $M > 7.0$ large deep earthquakes that have occurred from 1990 to 2023 (Fig. 1). We develop a hybrid subevent inversion method and model each deep earthquake as a sequence of point-source subevents, resolving their locations, timing, and focal mechanisms. This flexible parameterization can effectively resolve complex ruptures across multiple faults with varying geometries. In comparison to nonlinear Bayesian methods (*33–37*), our new method is computationally efficient, permitting systematic analysis of many large deep earthquakes. We linearly invert teleseismic P and SH waves to obtain moment tensor solutions of subevents for each earthquake. The location and timing of these subevents are characterized by an assumed unilateral rupture propagation, where we resolve the rupture directivity and velocity using a grid-search approach (see Materials and Methods). Physically, only a limited region will slip at any given time during an earthquake, and thus earthquake ruptures can be approximated as a few subevents (*36, 38, 39*). We overparameterize the inverse problem and apply this physics-based sparsity constraint to resolve the earthquake subevents (*40, 41*) (see Materials and Methods).

We model the subevents at the hypocentral depth of the earthquake (*12, 30, 42*). Most target earthquakes occurred in remote regions without stations directly above the events. This lack of nearby stations causes trade-offs between resolving the subevent timing and depth when solely using downgoing teleseismic body waves. Depth phases such as pP and sS phases provide insights into vertical rupture propagation (*33, 43*). However, the complexities of ocean bottom reflections, water reverberations, and heterogeneous subduction zones can significantly distort depth phases, limiting their capability for unified comparison of large deep earthquake ruptures. Fixing the subevents at the hypocentral depth can stabilize the inversion and is a useful approximation for robustly estimating the horizontal rupture length of the earthquakes (*12, 33*). We further validate our results by comparing our models with nine published models obtained using different methods, and the results are generally consistent (Fig. S1) (*11, 12, 30, 33, 44–46*).Additionally, we evaluate the influence of the vertical rupture extent, finding that it does not significantly affect our MOW analyses, which are discussed in more detail later. Robust estimates of the horizontal rupture length are critical for comparisons with the metastable olivine wedge geometry and assessing likely faulting mechanisms.

We find that 32 of the 40 target earthquakes require two or more subevents to explain their teleseismic body waves (Figs. 2–5 and S2). These subevent models suggest that few of the ruptures propagated parallel to the slab strike. Instead, the ruptures frequently penetrated through the interior of the slabs rather than being confined to the plate interface, such as for the 2013 Okhotsk M_W 8.3 (Fig. 2), the 1994 M_W 7.5 and 2018 M_W 8.2 Fiji deep earthquakes (Fig. 3), and the 1994 M_W 8.2 Bolivia earthquake (Fig. 5). The rupture lengths of these earthquakes vary from 10 to 70 kilometers (Figs. 2–5, S2), and the associated rupture velocities range from 1 to 5 km/s (Fig. S3–4). For example, the 1994 Fiji M_W 7.5 earthquake ruptured approximately 30 km with a fast rupture speed of 4 km/s (Figs. 3 and S4), while the 1994 Bolivia M_W 8.2 earthquake broke a fault area spanning approximately 20 km at a much slower rupture speed of 1 km/s (Fig. 5). The seismic moment of the 1994 Bolivia earthquake was 10 times that of the 1994 Fiji earthquake. The larger moment for the Bolivia event, occurring over a smaller fault dimension, implies a stress drop about 30 times greater than that of the Fiji earthquake, suggesting different rupture dynamics of these events.

We find that focal mechanisms of subevents can vary significantly for individual large deep earthquakes (Figs. 2–5). For example, the subevents can rotate their strike angles by over 50 degrees for the 1994 M_W 7.5, 2018 M_W 8.2 and 7.9 Fiji-Tonga, and 1996 M_W 7.7 Flores Sea deep earthquakes (Figs. 3–4). These subevent focal mechanism changes suggest that the earthquakes likely involved multiple episodes of rupture occurring on different faults with distinct geometries. We measure this variation in focal mechanisms of subevents for the 32 earthquakes with two or more subevents using their maximum 3D rotation angles between every pair of subevents (*47*). We find that the focal mechanism rotation angle tends to increase with earthquake magnitude (Fig. S4), suggesting that deep earthquakes of larger magnitudes may have been governed by different processes at the initiation and arresting stages.

Our subevent models agree with source models obtained using other datasets and techniques. The total seismic moment and the combined focal mechanisms of these subevents agree with the models from the Global Centroid-Moment-Tensor (GCMT) catalog (*3*) (Fig. S3). The total source durations inferred from the subevents also align well with the source time functions from the SCARDEC dataset (*48*) (Fig. S3). Their horizontal rupture lengths are in agreement with those in previous case studies (Fig. S1). To further understand the uncertainties in our earthquake models, we apply bootstrap resampling to estimate standard errors in the rupture velocity and length. We find the 90% confidential limits in rupture lengths are mostly within 20 km (Fig. S4).

We compare the horizontal rupture length of the 31 events with known slab geometries to the surrounding MOW widths. We resolve the MOW widths by conducting thermal simulations for subducting slabs where these deep earthquakes occurred, using a finite-element modeling method (*49*) and 2D cross section configurations specific for individual event (Fig. S5). We take the 725°C isotherm as the blocking temperature to track the metastable olivine at these subducting slabs (*18*). This blocking temperature represents a warmer bound in previous estimations (*50–52*), and decreasing this blocking temperature would yield thinner MOWs. Our simulations adopt realistic plate cooling model and other slab parameters, including geometries (*9*), slab ages, mantle temperature adiabats, and convergence rate (*53, 54*) (see Methods and supplementary materials for details). We also consider scenarios using a half-space cooling model and a larger adiabatic temperature gradient to represent the cold and warm end members of slab thermal models, to assess the uncertainty range in evaluating MOW widths relative to deep earthquake rupture extents. Our simulations show that the MOW exists within cold subducting slabs and its thickness decreases with depth, consistent with previous studies (*27, 55*). At 550 km depth, we obtain a MOW thickness of 15, 16, 25, and 11 km for the Tonga, Kuril, Bonin, and Java-Banda Sea subduction slabs, respectively (Figs. 6-7). Other warmer and younger subducting slabs, including the Honshu, Philippines, and South America slabs, have temperatures too high to permit coherent wedges of metastable olivine deeper than 500 km (Fig. 6).

We find that 25 of the 31 earthquakes likely ruptured beyond the model-predicted MOW width (Fig. 7), assuming the earthquakes initiated at the coldest core of the slab. Such a scenario was observed for the 2018 Fiji M_W 8.2 earthquake, which nucleated near the slab core and ruptured out of the MOW (*32, 33*). If we assume that the earthquakes started at one MOW edge and ruptured towards the other end, 20 earthquakes would have ruptured beyond the entire MOW width (Fig. 7g). For example, the 2013 Okhotsk M_W 8.3 earthquake ruptured approximately 65 km horizontally across the slab, four times greater than the predicted MOW thickness at a depth of 550 km. These events likely ruptured through the metastable olivine phase-transition boundary and extended into a thermal halo around the MOW, where ruptures appear to be able to propagate but earthquake nucleation may be prohibited (Fig. 7d-e). In warm slabs deficient in MOWs, such as the South American slab, the slab temperature and composition are highly heterogeneous, possibly aided by an abrupt increase in the age of the subducted slab at depths of 300-500 km (*56–58*). These heterogeneities may allow colder slab temperatures sporadically below these depths, leading to pockets of MOW where conditions are favorable. Earthquakes like the 1994 M_W 8.2 Bolivia event may nucleate at such isolated MOW pockets (*59–62*) and propagate into regions devoid of metastable olivine (Fig. 7f). For such earthquakes, mechanisms other than transformational faulting, possibly shear melting, are likely driving their rupture propagation.

Both the earthquake rupture extent and the width of metastable olivine wedges (MOW) estimates can have uncertainties. We systematically evaluate these uncertainties and find that they do not substantially impact our results. First, potential updip or downdip rupture of deep events might complicate comparisons of ruptures and MOWs. Previous studies indicate that large deep earthquake ruptures typically extend less than 20 km in depth (e.g. (*43, 63*)). We incorporate this extent into our analysis, and find neither shallowing nor downward ruptures significantly impact our observations of ruptures exceeding the MOWs (Fig. S8). Second, the blocking temperature for olivine metastability remains controversial with estimates ranging from 660°C (*52*) to the 725°C used in this study (*50, 51*). Adopting a lower blocking temperature of 660°C leads to thinner MOWs (Fig. S9), thereby supporting the observed discrepancies between rupture dimensions and MOWs. Finally, the choice of thermal modeling assumptions introduces additional uncertainty: using a half-space cooling model results in cooler temperatures and thicker MOWs than the plate cooling model used here, and applying an adiabatic gradient of 0.5°C/km yields warmer temperatures and thinner MOWs than the 0.3°C/km used in this study. However, considering these variations (Fig. 7g), our simulations indicate that the MOWs under both warm and cold thermal scenarios are insufficient to accommodate the observed deep earthquake rupture extents.

Dual mechanism transition enables larger final magnitude of deep earthquakes

Our observations indicate that $M > 7$ deep earthquakes are nucleated by the transformational faulting mechanism and transition to being governed by the thermal runaway process after their rupture propagates beyond the metastable olivine wedge. This transition process enables a larger final magnitude for these events. Deep earthquakes most likely nucleate by phase transitions of metastable olivine, as large deep earthquake sequences often show brittle-like characteristics by starting their ruptures with high rupture speed, high radiation efficiency, and moderate stress drop (*12, 13, 24, 32, 33*). Thermal runaway is unlikely to be a common initiating process for deep earthquakes because of a lack of a spontaneous mechanism for self-localization of shear thermal instability (*25, 64*). However, the thermal halo region is likely critically stressed as it is highly sensitive to external perturbations, where dynamic triggering of deep earthquakes occurs significantly more frequently than the MOW core (*65*). Our results show that about half of the $M > 7$ deep earthquakes occur in regions where slabs likely contain coherent MOW structures. The rest of the events might initiate in isolated MOW pockets when no coherent MOW is present. However, once deep earthquakes rupture beyond the confining MOW, their rupture, if continued, can be sustained by weakening processes due to shear melting. Once the rupture crosses the MOW boundary, local stress heterogeneity may not align with the faults caused by phase transitions of metastable olivine. Consequently, rupture planes may deviate from their initial configurations, leading to larger variations in subevent focal mechanisms for earthquakes of greater magnitude (Figs. 8-9).

Deep earthquakes caused by transformational faulting show moment release proportional to their size (*22*). This scaling relationship suggests that the transformational faulting process is comparable to brittle failure of shallow earthquakes (*66–68*). Consequently, deep earthquakes due to transformational faulting are likely to have little, if any, dependence of stress drop on moment. In contrast, the thermal runaway process can sustain earthquake rupture beyond the MOW boundary (thermal halo). However, the associated melting and large stress release could limit the rupture extent, and the moment release (earthquake slip) within the thermal halo is concentrated, disproportionate to its spatial length (*29, 31*).

Our findings show that the total rupture lengths of 32 of the large deep earthquakes do not follow the moment-length scaling relationship typically observed in crustal earthquakes, suggesting their ruptures were not solely controlled by the transformational faulting mechanism (Fig. 8). However, most of these earthquakes likely initiated in the cold slab cores, and this apparent paradox could be due to a dual control of both transformational faulting and thermal runaway mechanisms. The final earthquake magnitude hinges upon the transition of the mechanisms, and the transition is critical in releasing more moment and causing larger deep earthquakes ($M > 7.5$). For smaller events (e.g., $M < 7.5$), their ruptures are confined within the associated MOWs and their stress drop is approximately 10 MPa (Fig. 8). These stress drop estimates are comparable to those of crustal earthquakes (*10, 69, 70*). However, when earthquakes rupture beyond the MOW boundary and are sustained outside the MOW, they release most of their moment in the thermal halo, leading to larger magnitudes ($M > 7.5$). Our models show that stress drops of $M > 7.5$ deep earthquakes increase to 100 MPa on average, an order of magnitude greater than that of $M < 7.5$ earthquakes (Fig. 8). This difference between the smaller and larger events can also be seen in Fig. S2; the average rupture rupture length of the larger earthquakes is less than self-similar models predict based on the smaller earthquake rupture lengths, leading to bigger average stress drops for the larger earthquakes.

This stress drop-magnitude increase trend is robust to different assumptions for source scenarios (Fig. S6), and is also observed in global and Kuril deep earthquakes, whose stress drops estimates are obtained using different methods and datasets (*71–73*). Additionally, we find that the horizontal rupture velocities of large, deep earthquakes are in the range of 20%–90% of the local shear wave velocity, different from the typical 50%–90% fraction of the shear wave velocity for shallow earthquakes (Fig. S7). This difference is likely due to the partition of shear melting beyond the MOW boundary during the rupture processes of large deep earthquakes, which would slow down the rupture propagation (*31, 63, 74*).

Discussion

In addition to the transformational faulting and thermal runaway mechanisms, dehydration embrittlement has also been proposed to explain deep earthquakes (*75, 76*). However, this mechanism is challenged by the absence of an observable fluid release process (*1, 77*). Petrological analysis of diamonds originating from the mantle transition zone finds inclusions of hydrous minerals, indicating the presence of water at these depths (*78, 79*). However, water carried through the whole transition zone depths would be absorbed into the crystalline interfaces of the minerals, which do not migrate easily, causing the hydrous minerals to be stable for most slab conditions except regions with substantial slab folding and warming (*79*). This stability of hydrous minerals renders dehydration embrittlement less plausible for causing deep earthquakes below 500 km (*77*). In addition to metastable olivine, magnesite and enstatite may also transform into denser phases under the 500–700 km temperature and pressure conditions. These minerals, along with metastable olivine, might also be involved in transformational faulting (*68, 80*). Among this suite of minerals, olivine is most abundant in the upper mantle, and laboratory experiments of olivine under realistic deep-earthquake conditions have successfully reproduced faulting, earthquake nucleation, the Gutenberg-Richter distribution, and predominantly deviatoric moment tensors (*21, 22*). These findings support metastable olivine as the most likely mineral for the transformational faulting mechanism for deep earthquakes.

Subduction dynamics at 500 to 700 km depth are reflected by the stress conditions within and around the subduction slabs (*7, 81*). Focal mechanisms are useful in inferring these stress conditions (*82, 83*). However, the distribution of deep seismicity is associated with the extent of the MOW (*27*). The scarcity of seismic activity in the thermal halo outside of the MOW leaves the stress conditions at these parts of subduction slabs poorly understood. Our subevent models can provide a direct assessment of the moderate to small-scale stress environment in the thermal halos when deep earthquakes rupture beyond the MOWs. The focal mechanism rotations identified in our subevent models, spanning 10 to 70 km, agree in spatial pattern with the historical stress heterogeneities (Fig. S10). This indicates that the focal mechanism variations is due to a localized dual mechanism transition on the scale of kilometers, and the variations reflect a heterogeneous stress environment with changes occurring over tens to hundreds of kilometers (Fig. S10). These stress variations may arise from slab bending, structural heterogeneity, and adjacent mantle flow (*26, 84–86*). Our observed stress rotations may aid future numerical simulations for slab dynamics that account for more realistic stress environments and viscous resistance.

Materials and Methods

Earthquake Subevent Inversion: Data, Method, and Uncertainties

We develop a new multiple-subevent inversion method to determine the rupture process of large deep earthquakes. After assuming a rupture velocity and directivity, we parameterize the inverse problem using a series of spatial grids along a line indicating unilateral rupture propagation. Each grid is spaced by one second in rupture time, with a centroid moment tensor representing a potential subevent. We grid-search the optimal rupture directivity and rupture velocity based on the data misfit. We enforce a spatiotemporal sparsity constraint on the subevent centroid moment tensors using a mixed ℓ_{21} norm, where we first compute the ℓ_2 norm of the six moment tensor components of each grid point and them sum these values (ℓ_1) to derive a final penalty term.

$$\min \|Gm - d\|_2 + \beta \|m\|_{2,1} \tag{1}$$

where

$$\|m\|_{2,1} = \sum_{i=1}^{N} \sqrt{\sum_{j=1}^{6} (m_{ij}^2)} \tag{2}$$

We solve this inverse problem using the convex optimization tool CVX (*87*). This regularization balances the data misfit and the model sparsity. The strength of regularization, β, is obtained using L-curve analyses for the studied deep earthquakes. We further merge moment tensors of adjacent subevents that are less than 2 seconds apart. These regularization strategies resolve the complex rupture process of each large event as a few major subevents, grounded in the physical understanding that subevents represent major slip episodes during the rupture, and the larger subevents/asperities are the primary contributors to the overall rupture dynamics. We find that our subevent models can adequately describe rupture characteristics such as multi-fault ruptures and the rupture dimensions, and explain their teleseismic waves.

For each large deep earthquake, we invert teleseismic P and SH waves from global seismic networks II, IU, IC, G, GT, PS, to ensure relatively even azimuthal and distance coverage across the globe. We use an epicentral distance range of 30° to 90°. To effectively account for seismic energy distributed across various frequencies, we invert waves in displacement in the frequency domain using 32 frequency bands from 0.005–0.125 Hz. We compute synthetic seismograms using the Instaseis method (*88*), which uses pre-computed Green's functions computed from the AxiSEM method (*89*) and the anisotropic PREM velocity model up to 0.2 Hz resolution.

We estimate the rupture dimension of each large deep earthquake using the distance between the first and last subevents. To understand the uncertainties of the rupture dimensions, we adopt a bootstrapping resampling approach to each of the deep events investigated in this study. This involves repeatedly selecting a subset of both P and SH stations from the available data, where stations can be chosen multiple times (with replacement). For each resampled dataset, we perform new grid searches to estimate rupture velocity and directivity. We repeat this process 100 times for each deep event, estimate their distributions, and translate the 90% confidential interval of rupture velocities to the uncertainty of rupture dimensions.

Thermal Modeling of Subduction Slabs

We conduct thermal simulations for subducting slabs that host the analyzed global large deep earthquakes to assess the metastable olivine wedge structure at different subduction zones. We generate two-dimensional thermal models initialized from a plate cooling model (*90*) using updates to the digital grid of the age of oceanic plates (*53*), which represents the thermal state of the oceanic lithosphere at the beginning of the subduction processes. We model thermal profiles of 31 subduction zone transects across each large deep earthquake. The earthquakes have finite source dimensions and the source regions show spatial overlap with existing slab geometries (Fig. S5). For the slab surface geometry, we use the slab surface from the Slab2 model (*9*) for 22 transects except 9 transects in Tonga. For these 9 Tonga transects, we use the slab contours from the Reference Upper Mantle (RUM) model (*91*) as it provides better constraints on the unique geometry of the Tonga slab. The RUM geometry is more consistent with earthquake focal mechanisms than Slab2 model for these transects. We obtain plate convergence direction and velocity according to plate motion reconstruction since 200 Ma (*53*), and project the convergence velocity onto the transects (Table S2). We note that a variation of ±20 Ma in the plate age does not significantly change the temperature fields and MOW widths (Fig. S11). With these initial conditions for each subducting slab, we use high-resolution finite element modeling to estimate the thermal structure of the slabs (*49*), which incorporates a kinematic slab with known geometry as well as a dynamic mantle wedge with a composite rheology including both diffusion and dislocation creep.

The mantle potential temperature (T_p) and adiabatic temperature gradients have not been well constrained (*90, 92–95*). The associated uncertainties affect the deep slab mantle temperature among many other processes (*96*). Therefore, we performed a suite of thermal modeling analyses based on previously inferred mantle potential temperatures of 1300-1450°C and adiabatic temperature gradients of 0.3-0.5°C/km (*90, 93, 95*). The reference mantle potential temperature and adiabatic gradient we use are 1450°C and 0.3°C/km, respectively. When a higher adiabatic temperature gradient of 0.5°C/km is considered, the minimum slab temperature at 600 km depth of most subduction zone transects exceeds 725°C and no MOW would exit, which we take as a warm end-member. We argue this scenario is less plausible for most transects because MOW has been previously imaged seismically (*19, 20*). If we take the lower bound of mantle potential temperature of 1300°C, the MOW width at 550 km in the Tonga (15 km to 29 km), Kuril (16 km to 32 km), Bonin (25 km to 37 km), and Java-Banda (11 km to 30 km) all increase. We note that even for this cold scenario, the MOW width is still under 40 km for all subduction slabs at a depth of 550 km.

The half-space cooling model has been extensively used in geodynamic simulations due to its simplicity and capability to characterize oceanic plates cooling as they age. However, half-space cooling has its limitations as it assumes an infinite medium while only the lithosphere with finite thickness would cool effectively given effective upper mantle convection. Consequently, it could potentially underestimate the temperature of older incoming subduction slabs. Here we use a plate cooling model (*90*) in our thermal simulations, which incorporates a lithosphere of 50–km thickness, and thereby providing more realistic temperature estimates for subducting slabs. When using the half-space cooling, which represents the cold end member in slab thermal models, the MOWs at all earthquake source locations remains thinner than 40 km, which suggests most large deep earthquakes should still have ruptured beyond the MOW boundary.

References

1. H. W. Green, H. Houston, The mechanics of deep earthquakes. *Annual Review of Earth and Planetary Sciences* **23**, 169–213 (1995).

2. Z. Zhan, Mechanisms and implications of deep earthquakes. *Annual Review of Earth and Planetary Sciences* **48**, 147–174 (2020).

3. G. Ekström, M. Nettles, A. Dziewoński, The global CMT project 2004–2010: Centroid-moment tensors for 13,017 earthquakes. *Physics of the Earth and Planetary Interiors* **200**, 1–9 (2012).

4. B. Gutenberg, C. F. Richter, Earthquake magnitude, intensity, energy, and acceleration: (second paper). *Bulletin of the seismological society of America* **46**, 105–145 (1956).

5. C. Frohlich, The nature of deep-focus earthquakes. *Annual Review of Earth and Planetary Sciences* **17**, 227–254 (1989).

6. B. Isacks, P. Molnar, Distribution of stresses in the descending lithosphere from a global survey of focal-mechanism solutions of mantle earthquakes. *Reviews of Geophysics* **9**, 103–174 (1971).

7. M. I. Billen, Modeling the dynamics of subducting slabs. *Annu. Rev. Earth Planet. Sci.* **36**, 325–356 (2008).

8. R. Myhill, Slab buckling and its effect on the distributions and focal mechanisms of deep-focus earthquakes. *Geophysical Journal International* **192**, 837–853 (2013).

9. G. P. Hayes, G. L. Moore, D. E. Portner, M. Hearne, H. Flamme, M. Furtney, G. M. Smoczyk, Slab2, a comprehensive subduction zone geometry model. *Science* **362**, 58–61 (2018).

10. D. A. Wiens, J. J. McGuire, P. J. Shore, M. G. Bevis, K. Draunidalo, G. Prasad, S. P. Helu, A deep earthquake aftershock sequence and implications for the rupture mechanism of deep earthquakes. *Nature* **372**, 540–543 (1994).

11. R. Tibi, C. Estabrook, G. Bock, The 1996 June 17 Flores Sea and 1994 March 9 Fiji-Tonga earthquakes: source processes and deep earthquake mechanisms. *Geophysical Journal International* **138**, 625–642 (1999).

12. Z. Zhan, H. Kanamori, V. C. Tsai, D. V. Helmberger, S. Wei, Rupture complexity of the 1994 Bolivia and 2013 Sea of Okhotsk deep earthquakes. *Earth and Planetary Science Letters* **385**, 89–96 (2014).

13. L. Ye, T. Lay, H. Kanamori, K. D. Koper, Energy release of the 2013 Mw 8.3 Sea of Okhotsk earthquake and deep slab stress heterogeneity. *Science* **341**, 1380–1384 (2013).

14. S. H. Kirby, Localized polymorphic phase transformations in high-pressure faults and applications to the physical mechanism of deep earthquakes. *Journal of Geophysical Research: Solid Earth* **92**, 13789–13800 (1987).

15. H. W. Green, P. Burnley, A new self-organizing mechanism for deep-focus earthquakes. *Nature* **341**, 733–737 (1989).

16. P. C. Burnley, H. W. Green, D. J. Prior, Faulting associated with the olivine to spinel transformation in Mg2Geo4 and its implications for deep-focus earthquakes. *Journal of Geophysical Research: Solid Earth* **96**, 425–443 (1991).

17. H. Schmeling, R. Monz, D. C. Rubie, The influence of olivine metastability on the dynamics of subduction. *Earth and Planetary Science Letters* **165**, 55–66 (1999).

18. J. Quinteros, S. V. Sobolev, Constraining kinetics of metastable olivine in the marianas slab from seismic observations and dynamic models. *Tectonophysics* **526**, 48–55 (2012).

19. H. Kawakatsu, S. Yoshioka, Metastable olivine wedge and deep dry cold slab beneath southwest Japan. *Earth and Planetary Science Letters* **303**, 1–10 (2011).

20. Z. Shen, Z. Zhan, Metastable olivine wedge beneath the Japan Sea imaged by seismic interferometry. *Geophysical Research Letters* **47**, e2019GL085665 (2020).

21. A. Schubnel, F. Brunet, N. Hilairet, J. Gasc, Y. Wang, H. W. Green, Deep-focus earthquake analogs recorded at high pressure and temperature in the laboratory. *Science* **341**, 1377–1380 (2013).

22. Y. Wang, L. Zhu, F. Shi, A. Schubnel, N. Hilairet, T. Yu, M. Rivers, J. Gasc, A. Addad, D. Deldicque, *et al.*, A laboratory nanoseismological study on deep-focus earthquake micromechanics. *Science Advances* **3**, e1601896 (2017).

23. J. J. McGuire, D. A. Wiens, P. J. Shore, M. G. Bevis, The march 9, 1994 (Mw 7.6), deep Tonga earthquake: Rupture outside the seismically active slab. *Journal of Geophysical Research: Solid Earth* **102**, 15163–15182 (1997).

24. L. Meng, J.-P. Ampuero, R. Bürgmann, The 2013 Okhotsk deep-focus earthquake: Rupture beyond the metastable olivine wedge and thermally controlled rise time near the edge of a slab. *Geophysical Research Letters* **41**, 3779–3785 (2014).

25. M. Ogawa, Shear instability in a viscoelastic material as the cause of deep focus earthquakes. *Journal of Geophysical Research: Solid Earth* **92**, 13801–13810 (1987).

26. S. Karato, M. R. Riedel, D. A. Yuen, Rheological structure and deformation of subducted slabs in the mantle transition zone: implications for mantle circulation and deep earthquakes. *Physics of the Earth and Planetary Interiors* **127**, 83–108 (2001).

27. S. H. Kirby, S. Stein, E. A. Okal, D. C. Rubie, Metastable mantle phase transformations and deep earthquakes in subducting oceanic lithosphere. *Reviews of geophysics* **34**, 261–306 (1996).

28. J. L. Mosenfelder, F. C. Marton, C. R. Ross II, L. Kerschhofer, D. C. Rubie, Experimental constraints on the depth of olivine metastability in subducting lithosphere. *Physics of the Earth and Planetary Interiors* **127**, 165–180 (2001).

29. P. G. Silver, S. L. Beck, T. C. Wallace, C. Meade, S. C. Myers, D. E. James, R. Kuehnel, Rupture characteristics of the deep Bolivian earthquake of 9 June 1994 and the mechanism of deep-focus earthquakes. *Science* **268**, 69–73 (1995).

30. M. Kikuchi, H. Kanamori, The mechanism of the deep Bolivia earthquake of June 9, 1994. *Geophysical Research Letters* **21**, 2341–2344 (1994).

31. H. Kanamori, D. L. Anderson, T. H. Heaton, Frictional melting during the rupture of the 1994 Bolivian earthquake. *Science* **279**, 839–842 (1998).

32. W. Fan, S. S. Wei, D. Tian, J. J. McGuire, D. A. Wiens, Complex and diverse rupture processes of the 2018 Mw 8.2 and Mw 7.9 Tonga-Fiji deep earthquakes. *Geophysical Research Letters* **46**, 2434–2448 (2019).

33. Z. Jia, Z. Shen, Z. Zhan, C. Li, Z. Peng, M. Gurnis, The 2018 Fiji Mw 8.2 and 7.9 deep earthquakes: One doublet in two slabs. *Earth and Planetary Science Letters* **531**, 115997 (2020).

34. Z. Jia, X. Wang, Z. Zhan, Multifault models of the 2019 Ridgecrest sequence highlight complementary slip and fault junction instability. *Geophysical Research Letters* **47**, e2020GL089802 (2020).

35. Z. Jia, Z. Zhan, H. Kanamori, The 2021 South Sandwich Island Mw 8.2 earthquake: A slow event sandwiched between regular ruptures. *Geophysical Research Letters* **49**, e2021GL097104 (2022).

36. M. Kikuchi, H. Kanamori, Inversion of complex body waves—III. *Bulletin of the Seismological Society of America* **81**, 2335–2350 (1991).

37. Q. Shi, S. Wei, M. Chen, An MCMC multiple point sources inversion scheme and its application to the 2016 Kumamoto Mw 6.2 earthquake. *Geophysical Journal International* **215**, 737–752 (2018).

38. T. Lay, H. Kanamori, C. J. Ammon, K. D. Koper, A. R. Hutko, L. Ye, H. Yue, T. M. Rushing, Depth-varying rupture properties of subduction zone megathrust faults. *Journal of Geophysical Research: Solid Earth* **117** (2012).

39. H. Yue, T. Lay, Resolving complicated faulting process using multi-point-source representation: Iterative inversion algorithm improvement and application to recent complex earthquakes. *Journal of Geophysical Research: Solid Earth* **125**, e2019JB018601 (2020).

40. H. Yao, P. Gerstoft, P. M. Shearer, C. Mecklenbräuker, Compressive sensing of the Tohoku-Oki Mw 9.0 earthquake: Frequency-dependent rupture modes. *Geophysical Research Letters* **38** (2011).

41. W. Fan, P. M. Shearer, P. Gerstoft, Kinematic earthquake rupture inversion in the frequency domain. *Geophysical Journal International* **199**, 1138 (2014).

42. S. Goes, J. Ritsema, A broadband P wave analysis of the large deep Fiji Island and Bolivia earthquakes of 1994. *Geophysical research letters* **22**, 2249–2252 (1995).

43. Y. Chen, L. Wen, Global large deep-focus earthquakes: Source process and cascading failure of shear instability as a unified physical mechanism. *Earth and Planetary Science Letters* **423**, 134–144 (2015).

44. S. Wei, D. Helmberger, Z. Zhan, R. Graves, Rupture complexity of the Mw 8.3 Sea of Okhotsk earthquake: Rapid triggering of complementary earthquakes? *Geophysical Research Letters* **40**, 5034–5039 (2013).

45. L. Ye, T. Lay, Z. Zhan, H. Kanamori, J.-L. Hao, The isolated 680 km deep 30 May 2015 Mw 7.9 Ogasawara (Bonin) Islands earthquake. *Earth and Planetary Science Letters* **433**, 169–179 (2016).

46. L. Ye, T. Lay, H. Kanamori, Z. Zhan, Z. Duputel, Diverse rupture processes in the 2015 Peru deep earthquake doublet. *Science Advances* **2**, e1600581 (2016).

47. Y. Kagan, 3-D rotation of double-couple earthquake sources. *Geophysical Journal International* **106**, 709–716 (1991).

48. M. Vallée, V. Douet, A new database of source time functions (STFs) extracted from the SCARDEC method. *Physics of the Earth and Planetary Interiors* **257**, 149–157 (2016).

49. N. Sime, C. R. Wilson, P. E. van Keken, Thermal modeling of subduction zones with prescribed and evolving 2d and 3d slab geometries. *Progress in Earth and Planetary Science* **11**, 14 (2024).

50. S. Yoshioka, Y. Torii, M. R. Riedel, Impact of phase change kinetics on the Mariana slab within the framework of 2-D mantle convection. *Physics of the Earth and Planetary Interiors* **240**, 70–81 (2015).

51. M. Tetzlaff, H. Schmeling, The influence of olivine metastability on deep subduction of oceanic lithosphere. *Physics of the Earth and Planetary Interiors* **120**, 29–38 (2000).

52. D. C. Rubie, C. R. Ross II, Kinetics of the olivine-spinel transformation in subducting lithosphere: Experimental constraints and implications for deep slab processes. *Physics of the Earth and Planetary Interiors* **86**, 223–243 (1994).

53. M. Seton, R. D. Müller, S. Zahirovic, C. Gaina, T. Torsvik, G. Shephard, A. Talsma, M. Gurnis, M. Turner, S. Maus, *et al.*, Global continental and ocean basin reconstructions since 200 Ma. *Earth-Science Reviews* **113**, 212–270 (2012).

54. E. M. Syracuse, P. E. van Keken, G. A. Abers, The global range of subduction zone thermal models. *Physics of the Earth and Planetary Interiors* **183**, 73–90 (2010).

55. C. Marone, M. Liu, Transformation shear instability and the seismogenic zone for deep earthquakes. *Geophysical Research Letters* **24**, 1887–1890 (1997).

56. D. Engebretson, S. Kirby, Deep Nazca slab seismicity: why is it so anomalous. *Eos, Trans. Am. Geophys. Un* **73**, 379 (1992).

57. S. H. Kirby, E. A. Okal, E. R. Engdahl, The 9 June 94 Bolivian deep earthquake: An exceptional event in an extraordinary subduction zone. *Geophysical Research Letters* **22**, 2233–2236 (1995).

58. J. Collier, G. Helffrich, The thermal influence of the subducting slab beneath South America from 410 and 660 km discontinuity observations. *Geophysical Journal International* **147**, 319–329 (2001).

59. M. R. Brudzinski, W.-P. Chen, Earthquakes and strain in subhorizontal slabs. *Journal of Geophysical Research: Solid Earth* **110** (2005).

60. J. E. Vidale, H. M. Benz, Upper-mantle seismic discontinuities and the thermal structure of subduction zones. *Nature* **356**, 678–683 (1992).

61. M. Tetzlaff, H. Schmeling, Time-dependent interaction between subduction dynamics and phase transition kinetics. *Geophysical Journal International* **178**, 826–844 (2009).

62. E. A. Okal, S. H. Kirby, Deep earthquakes beneath the Fiji basin, SW Pacific: Earth's most intense deep seismicity in stagnant slabs. *Physics of the Earth and Planetary Interiors* **109**, 25–63 (1998).

63. R. Tibi, G. Bock, D. A. Wiens, Source characteristics of large deep earthquakes: Constraint on the faulting mechanism at great depths. *Journal of Geophysical Research: Solid Earth* **108** (2003).

64. P. B. Kelemen, G. Hirth, A periodic shear-heating mechanism for intermediate-depth earthquakes in the mantle. *Nature* **446**, 787–790 (2007).

65. Y. Luo, D. A. Wiens, High rates of deep earthquake dynamic triggering in the thermal halos of subducting slabs. *Geophysical Research Letters* **47**, e2019GL086125 (2020).

66. M. Vallée, Source time function properties indicate a strain drop independent of earthquake depth and magnitude. *Nature communications* **4**, 2606 (2013).

67. X. Cui, Z. Li, Y. Hu, Similar seismic moment release process for shallow and deep earthquakes. *Nature Geoscience* pp. 1–7 (2023).

68. J. Li, Y. Zheng, L. Thomsen, T. J. Lapen, X. Fang, Deep earthquakes in subducting slabs hosted in highly anisotropic rock fabric. *Nature Geoscience* **11**, 696–700 (2018).

69. H. Houston, Q. Williams, Fast rise times and the physical mechanism of deep earthquakes. *Nature* **352**, 520 (1991).

70. P. M. Shearer, R. E. Abercrombie, D. T. Trugman, Improved stress drop estimates for M 1.5 to 4 earthquakes in southern California from 1996 to 2019. *Journal of Geophysical Research: Solid Earth* **127**, e2022JB024243 (2022).

71. M. Liu, Y. Huang, J. Ritsema, Stress drop variation of deep-focus earthquakes based on empirical Green's functions. *Geophysical Research Letters* **47**, e2019GL086055 (2020).

72. A. R. Turner, A. M. Ferreira, A. Berbellini, N. Brantut, M. Faccenda, E. Kendall, Across-slab propagation and low stress drops of deep earthquakes in the Kuril subduction zone. *Geophysical Research Letters* **49**, e2022GL098402 (2022).

73. Q. Shi, M. A. Denolle, Improved observations of deep earthquake ruptures using machine learning. *Journal of Geophysical Research: Solid Earth* **128**, e2023JB027334 (2023).

74. D. A. Wiens, Seismological constraints on the mechanism of deep earthquakes: Temperature dependence of deep earthquake source properties. *Physics of the Earth and Planetary Interiors* **127**, 145–163 (2001).

75. S. Omori, T. Komabayashi, S. Maruyama, Dehydration and earthquakes in the subducting slab: Empirical link in intermediate and deep seismic zones. *Physics of the Earth and Planetary Interiors* **146**, 297–311 (2004).

76. C. Meade, R. Jeanloz, Deep-focus earthquakes and recycling of water into the Earth's mantle. *Science* **252**, 68–72 (1991).

77. H. W. Green, W.-P. Chen, M. R. Brudzinski, Seismic evidence of negligible water carried below 400-km depth in subducting lithosphere. *Nature* **467**, 828–831 (2010).

78. D. Pearson, F. Brenker, F. Nestola, J. McNeill, L. Nasdala, M. Hutchison, S. Matveev, K. Mather, G. Silversmit, S. Schmitz, *et al.*, Hydrous mantle transition zone indicated by ringwoodite included within diamond. *Nature* **507**, 221–224 (2014).

79. S. B. Shirey, L. S. Wagner, M. J. Walter, D. G. Pearson, P. E. van Keken, Slab transport of fluids to deep focus earthquake depths–thermal modeling constraints and evidence from diamonds. *AGU Advances* **2**, e2020AV000304 (2021).

80. A. Hogrefe, D. Rubie, T. Sharp, F. Seifert, Metastability of enstatite in deep subducting lithosphere. *Nature* **372**, 351–353 (1994).

81. L. Alisic, M. Gurnis, G. Stadler, C. Burstedde, L. C. Wilcox, O. Ghattas, Slab stress and strain rate as constraints on global mantle flow. *Geophysical Research Letters* **37** (2010).

82. L. M. Warren, E. C. Baluyut, T. Osburg, K. Lisac, S. Kokkinen, Fault plane orientations of intermediate-depth and deep-focus earthquakes in the Japan-Kuril-Kamchatka subduction zone. *Journal of Geophysical Research: Solid Earth* **120**, 8366–8382 (2015).

83. Y. Chang, L. Warren, L. Zhu, G. Prieto, Earthquake focal mechanisms and stress field for the intermediate-depth Cauca cluster, Colombia. *Journal of Geophysical Research: Solid Earth* **124**, 822–836 (2019).

84. F. A. Capitanio, M. Faccenda, Complex mantle flow around heterogeneous subducting oceanic plates. *Earth and Planetary Science Letters* **353**, 29–37 (2012).

85. M. I. Billen, Deep slab seismicity limited by rate of deformation in the transition zone. *Science Advances* **6**, eaaz7692 (2020).

86. H. Liu, M. Gurnis, W. Leng, Z. Jia, Z. Zhan, Tonga slab morphology and stress variations controlled by a relic slab: Implications for deep earthquakes in the Tonga-Fiji region. *Geophysical Research Letters* **48**, e2020GL091331 (2021).

87. M. Grant, S. Boyd, Y. Ye, *Disciplined convex programming* (Springer, 2006).

88. M. Van Driel, L. Krischer, S. C. Stähler, K. Hosseini, T. Nissen-Meyer, Instaseis: instant global seismograms based on a broadband waveform database. *Solid Earth* **6**, 701–717 (2015).

89. T. Nissen-Meyer, M. Van Driel, S. C. Stähler, K. Hosseini, S. Hempel, L. Auer, A. Colombi, A. Fournier, AxiSEM: broadband 3-D seismic wavefields in axisymmetric media. *Solid Earth* **5**, 425–445 (2014).

90. C. A. Stein, S. Stein, A model for the global variation in oceanic depth and heat flow with lithospheric age. *Nature* **359**, 123–129 (1992).

91. Ó. Gudmundsson, M. Sambridge, A regionalized upper mantle (RUM) seismic model. *Journal of Geophysical Research: Solid Earth* **103**, 7121–7136 (1998).

92. J. M. Brown, T. J. Shankland, Thermodynamic parameters in the Earth as determined from seismic profiles. *Geophysical Journal International* **66**, 579–596 (1981).

93. D. L. Turcotte, G. Schubert, *Geodynamics* (Cambridge University Press, 2002), second edn.

94. F. D. Stacey, P. M. Davis, *Physics of the Earth* (Cambridge University Press, 2008).

95. T. Katsura, A. Yoneda, D. Yamazaki, T. Yoshino, E. Ito, Adiabatic temperature profile in the mantle. *Physics of the Earth and Planetary Interiors* **183**, 212–218 (2010).

96. W. Leng, W. Mao, Geodynamic modeling of thermal structure of subduction zones. *Science China Earth Sciences* **58**, 1070–1083 (2015).

97. J. D. Eshelby, The determination of the elastic field of an ellipsoidal inclusion, and related problems. *Proceedings of the Royal Society of London. Series A. Mathematical and Physical Sciences* **241**, 376–396 (1957).

98. Y. Kaneko, P. Shearer, Variability of seismic source spectra, estimated stress drop, and radiated energy, derived from cohesive-zone models of symmetrical and asymmetrical circular and elliptical ruptures. *Journal of Geophysical Research: Solid Earth* **120**, 1053–1079 (2015).

99. P. E. van Keken, C. R. Wilson, An introductory review of the thermal structure of subduction zones: I–motivation and selected examples. *Progress in Earth and Planetary Science* **10**, 42 (2023).

100. P. E. van Keken, C. R. Wilson, An introductory review of the thermal structure of subduction zones: III–Comparison between models and observations. *Progress in Earth and Planetary Science* **10**, 57 (2023).

101. N. Sime, C. R. Wilson, P. E. van Keken, Thermal modeling of subduction zones with prescribed and evolving 2D and 3D slab geometries data (2024).

102. P. E. van Keken, C. Currie, S. D. King, M. D. Behn, A. Cagnioncle, J. He, R. F. Katz, S.-C. Lin, E. M. Parmentier, M. Spiegelman, K. Wang, A community benchmark for subduction zone modeling. *Physics of the Earth and Planetary Interiors* **171**, 187–197 (2008).

103. S. I. Karato, P. Wu, Rheology of the upper mantle: A synthesis. *Science* **260**, 771–778 (1993).

104. D. Melgar, G. P. Hayes, Systematic observations of the slip pulse properties of large earthquake ruptures. *Geophysical Research Letters* **44**, 9691–9698 (2017).

Acknowledgements: The facilities of IRIS Data Services, and specifically the IRIS Data Management Center, were used for access to seismic waveforms recorded by global seismic networks II, IU, IC, G, GT, PS, the related metadata, and/or derived products used in this study. We thank Heidi Houston, Zhongwen Zhan, Lara Wagner, Alice Gabriel for helpful discussions. We thank Douglas Wiens and another anonymous reviewer for constructive review comments.
Funding: This work is supported by the United States Geological Survey grant G22AP00011, and the Cecil and Ida Green Foundation. DM was supported by the National Science Foundation through grant Nos. EAR-2121568 and OAC-2311208.
Author Contributions ZJ and WF conceptualized and led this study. ZJ, WF, and PS developed the subevent inversion method. ZJ conducted the subevent and stress drop analyses. WM conducted the thermal simulations. DM supervised the uncertainty analysis of thermal models.

ZJ wrote the original draft. All authors contributed to reviewing and editing.

Competing Interests Authors declare no competing interests.

Data and materials availability: All seismic data used in this study are publicly available from the IRIS-DMC. All subevent and thermal models are publicly available from https://utexas.box.com/s/w4rj78ck87na3pxnnzppkvtby7qzddai.

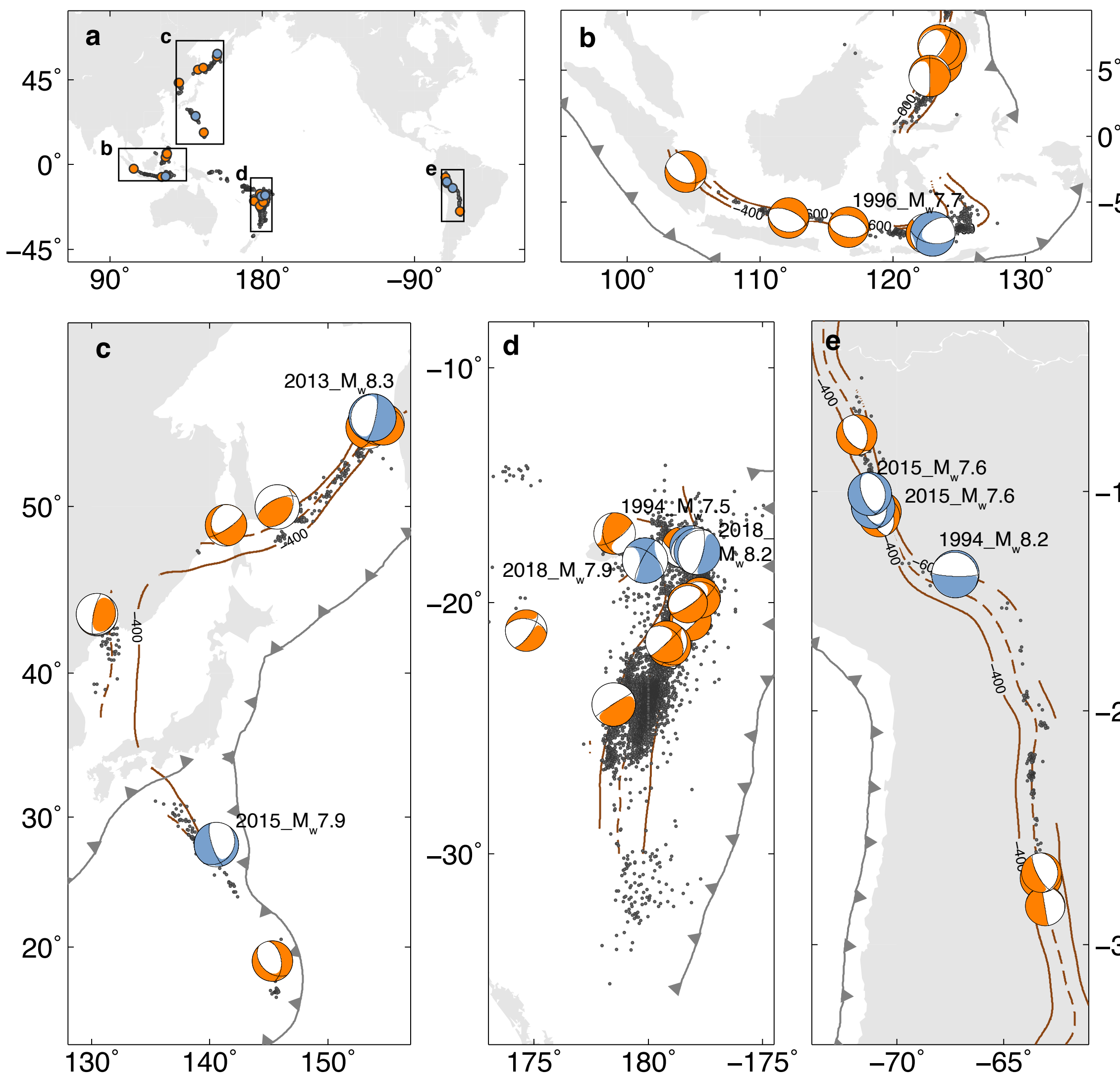
a
b
c
d
e
45°
0°
−45°
90°
180°
−90°
5°
0°
−5°
100°
110°
120°
130°
1996_M$_w$7.7
2013_M$_w$8.3
2015_M$_w$7.9
50°
40°
30°
20°
130°
140°
150°
−10°
−20°
−30°
175°
180°
−175°
1994_M$_w$7.5
2018_M$_w$8.2
2018_M$_w$7.9
2015_M$_w$7.6
2015_M$_w$7.6
1994_M$_w$8.2
−70°
−65°

642

Fig. 1. Global deep earthquakes with moment magnitude greater than 7.0 from 1990–2023. (a) Global distribution of analyzed large deep earthquakes, indicated by blue and orange circles. Subsequent panels detail the events in (b) Sumatra-Philippines, (c) Kuril-Honshu-Bonin, (d) Tonga, and (e) South America subduction zones. Focal mechanisms (beachballs) are from the Global Centroid Moment Tensor (GCMT) catalog. Events analyzed in previous case studies are colored in blue. Black dots indicate the historical deep (500 to 700 km) seismicity in the study regions. Slab depth contours are from the Slab 2 model (*9*).

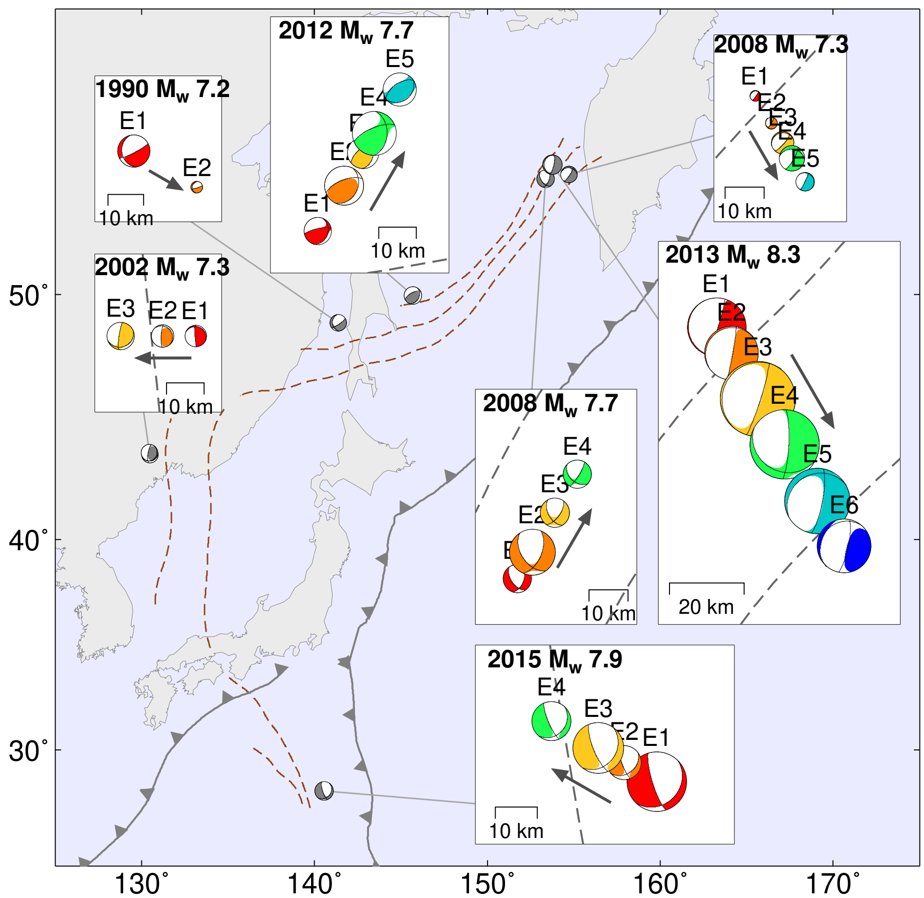

1990 Mw 7.2
E1
E2
10 km
2012 Mw 7.7
E5
E4
E1
10 km
2008 Mw 7.3
E1
E2
E3
E4
E5
10 km
2002 Mw 7.3
E3
E2
E1
10 km
2013 Mw 8.3
E1
E2
E3
E4
E5
E6
20 km
2008 Mw 7.7
E4
E3
E2
10 km
2015 Mw 7.9
E4
E3
E2
E1
10 km
50°
40°
30°
130°
140°
150°
160°
170°

650

Fig. 2. Subevent models of seven large deep earthquakes in the Kuril-Honshu-Bonin regions. Gray beachballs show the GCMT solutions for these events. Inset boxes show the subevent models for the corresponding earthquakes, where beachballs indicate the focal mechanisms and locations of subevents. The beachball size scales with seismic moment for each subevent. Gray arrows show the rupture directivity. Slab depth contours are from the Slab 2 model (*9*)

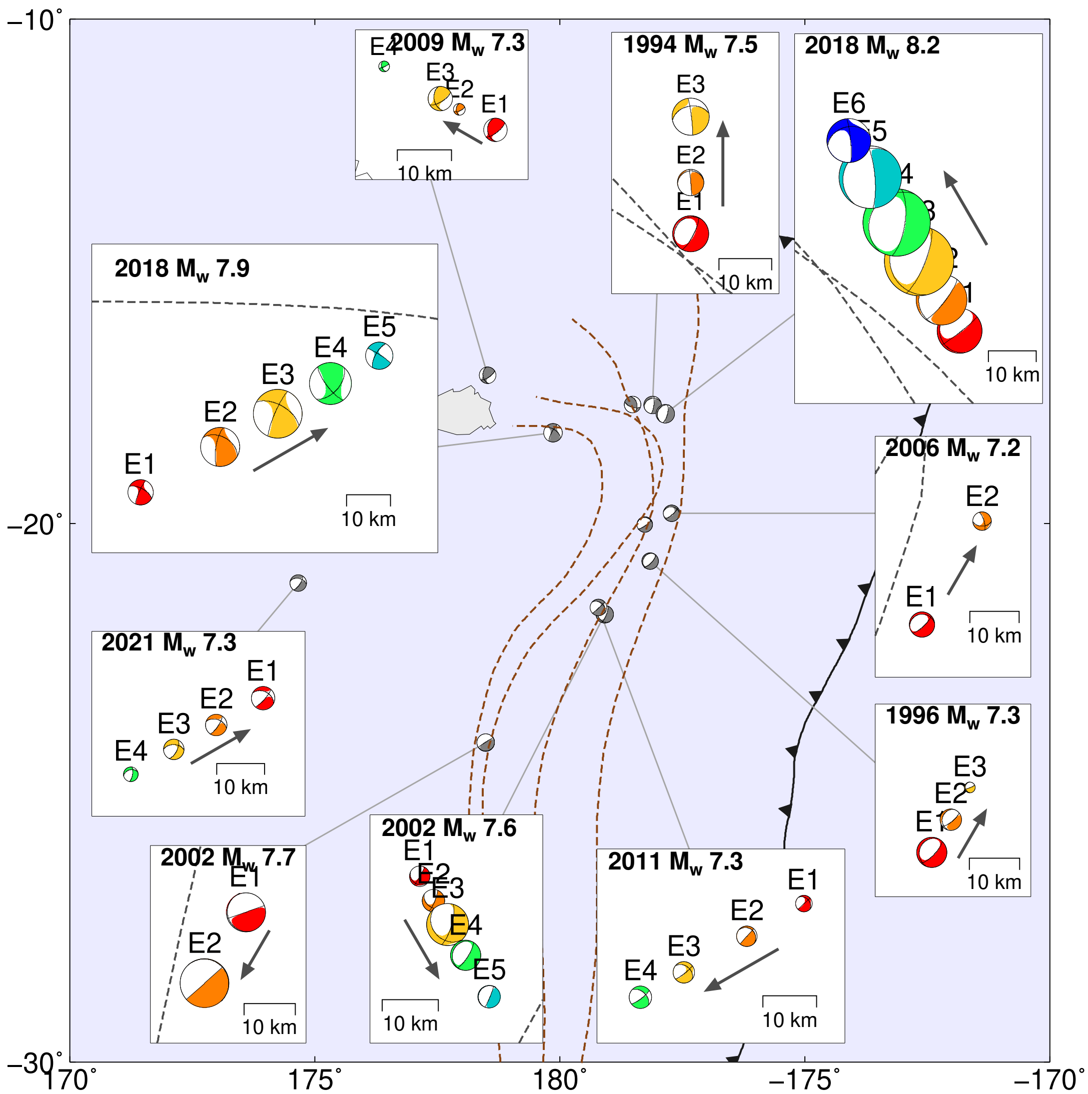
2009 Mw 7.3
1994 Mw 7.5
2018 Mw 8.2
2018 Mw 7.9
2006 Mw 7.2
1996 Mw 7.3
2021 Mw 7.3
2002 Mw 7.7
2002 Mw 7.6
2011 Mw 7.3
10 km
−10˚
−20˚
−30˚
170˚
175˚
180˚
−175˚
−170˚

656

Fig. 3. Subevent models of 11 large deep earthquakes in the Tonga subduction zone. Legends are similar to those in Fig. 2, except that slab depth contours are from the RUM model (*91*).

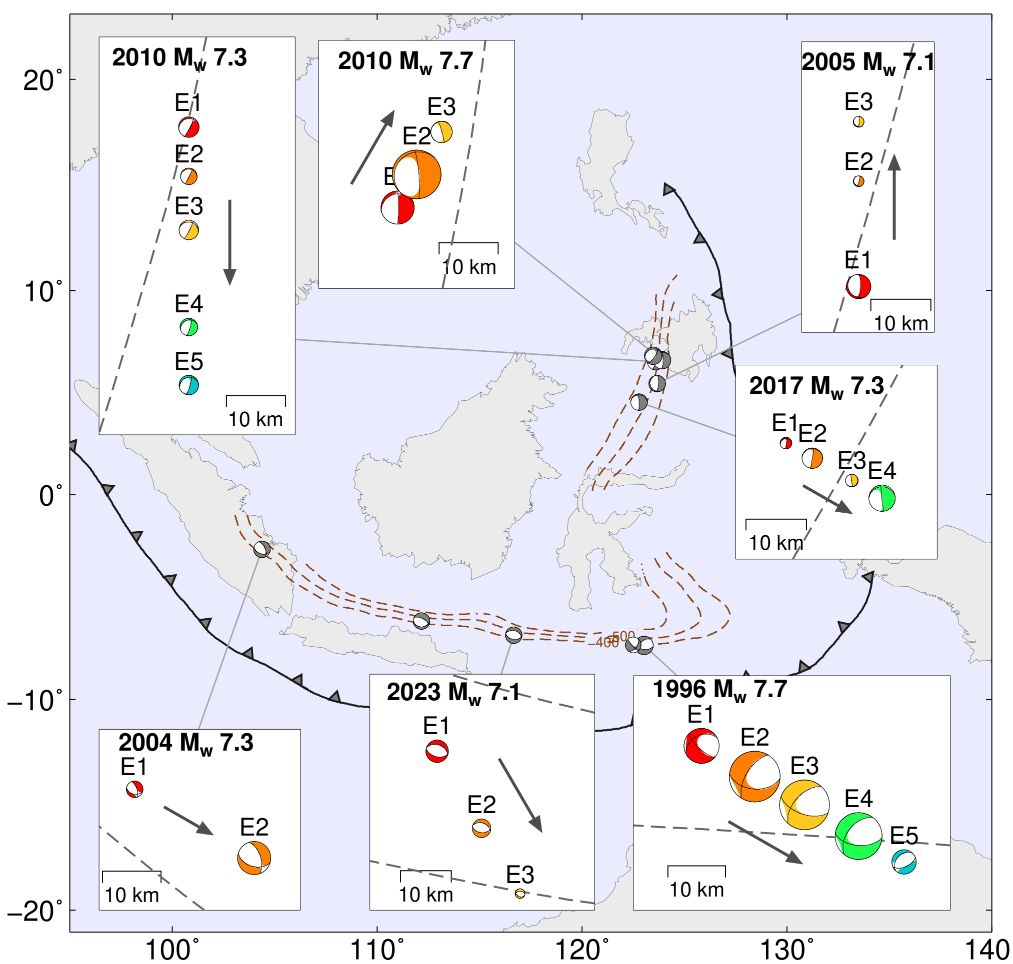
2010 M_w 7.3
E1
E2
E3
E4
E5
10 km
2010 M_w 7.7
E3
E2
10 km
2005 M_w 7.1
E3
E2
E1
10 km
2017 M_w 7.3
E1
E2
E3
E4
10 km
2004 M_w 7.3
E1
E2
10 km
2023 M_w 7.1
E1
E2
E3
10 km
1996 M_w 7.7
E1
E2
E3
E4
E5
10 km
20°
10°
0°
−10°
−20°
100°
110°
120°
130°
140°

659

Fig. 4. Subevent models of six large deep earthquakes in the Philippines and Sumatra subduction zones. Legends are similar to those in Fig. 2.

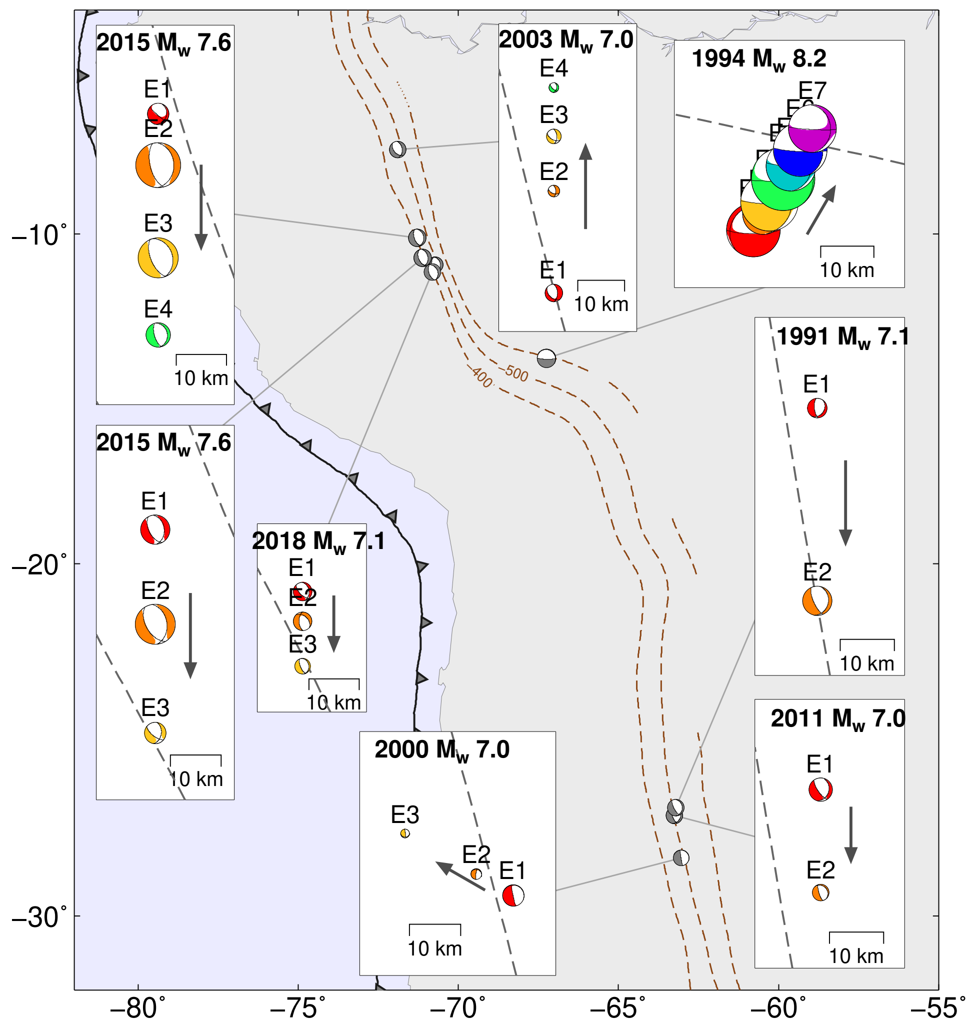

2015 Mw 7.6
E1
E2
E3
E4
10 km
2003 Mw 7.0
E4
E3
E2
E1
10 km
1994 Mw 8.2
E7
10 km
1991 Mw 7.1
E1
E2
10 km
2015 Mw 7.6
E1
E2
E3
10 km
2018 Mw 7.1
E1
E2
E3
10 km
2000 Mw 7.0
E3
E2
E1
10 km
2011 Mw 7.0
E1
E2
10 km
-500
-400
−10˚
−20˚
−30˚
−80˚
−75˚
−70˚
−65˚
−60˚
−55˚

662

Fig. 5. Subevent models of eight large deep earthquakes in the southern America subduction zone. Legends are similar to those in Fig. 2.

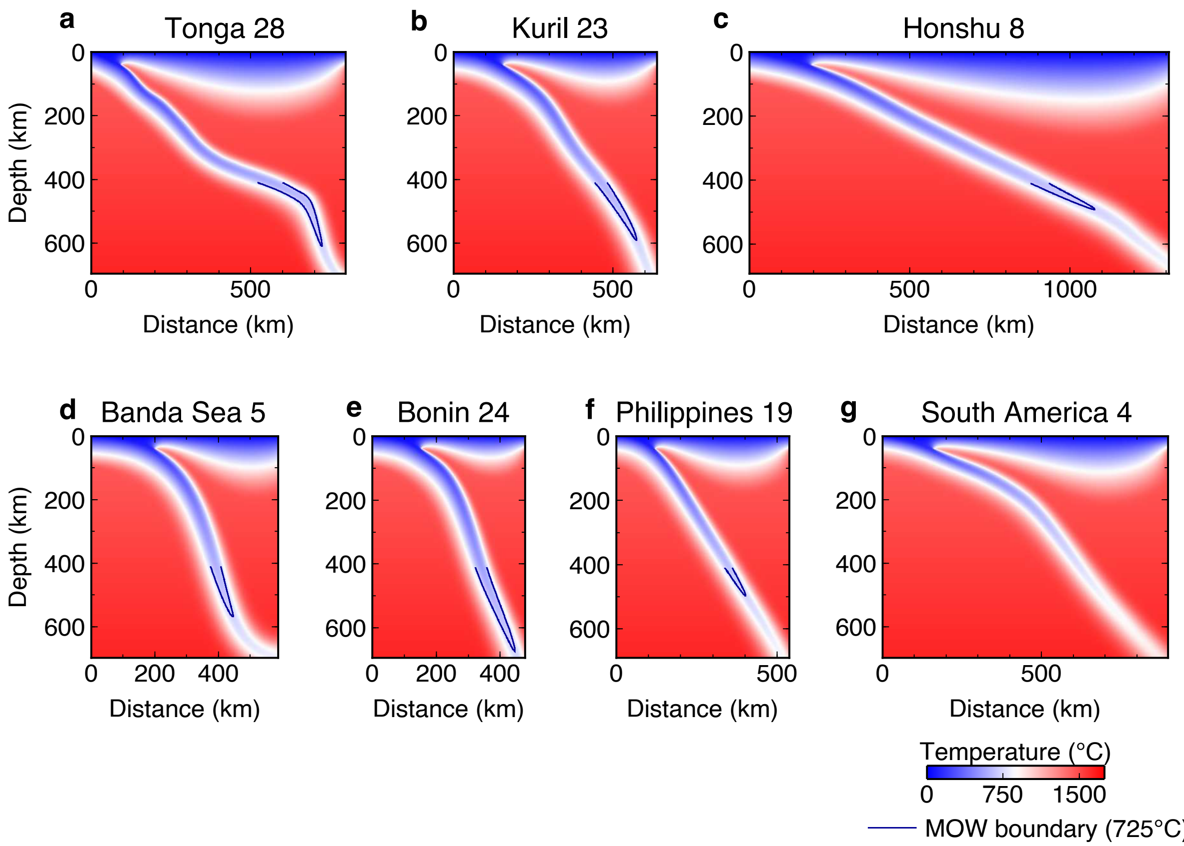

Fig. 6. Thermal models of seven subduction slabs. These models have a mantle temperature of 1450°C with an adiabatic gradient of 0.3°C/km. Numbers correspond to 2D transects in Fig. S5. Blue lines indicate the inferred boundary for a 99% metastable olivine phase transformation, based on a blocking temperature of 725°C.

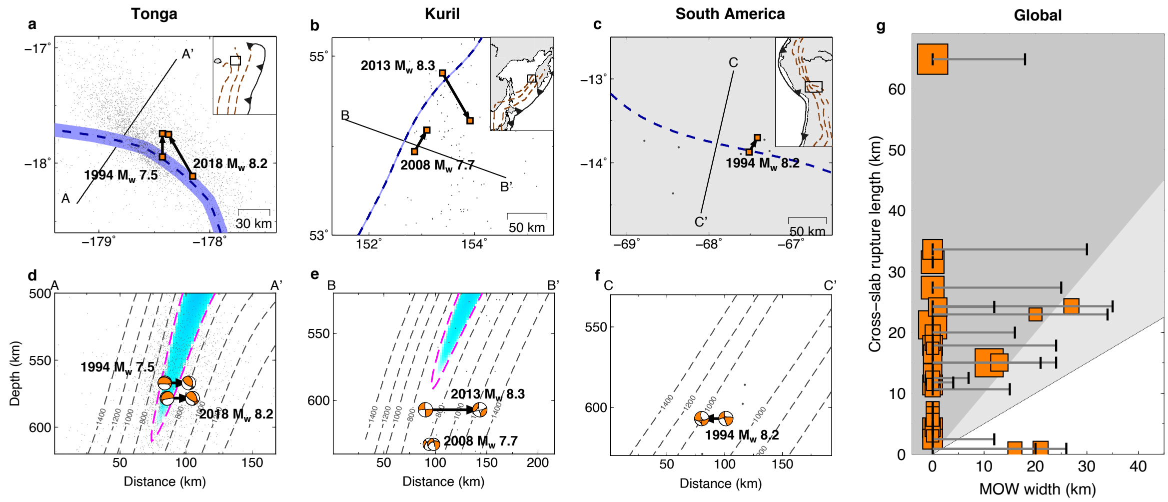

Fig. 7. Examples of large deep earthquakes that rupture beyond the metastable olivine wedges. (a–c) Map views showing the rupture extents of large deep earthquakes (marked by orange squares for initiating and ending subevents) and the metastable olivine wedge (MOW) (blue belts) at 600 km depth in (a) Tonga, (b) Kuril, and (c) South America. Dashed blue lines represent the inferred coldest slab cores based on the RUM (for Tonga) and slab2 (for other slabs) contours at a depth of 600 km. Gray dots denote historical seismicity in these regions. (d–f) Cross-section views of the rupture extents (beachballs connected by arrows) and the MOW (blue colored area). Dashed gray lines represent isotherm contours from thermal simulations. (g) Large deep earthquake rupture extents and the metastable olivine wedge width. Rupture extents are projected across the slabs and metastable olivine wedge widths are inferred from thermal models. Each earthquake is represented by an orange square with size proportional to the moment magnitude. The error bars indicate the MOW widths as derived from the cold and warm end-member slab models. The gray area highlights events with rupture extents that exceed the full width of the MOW. The light gray area indicates events that would have ruptured outside the MOWs if they nucleated at the MOW center.

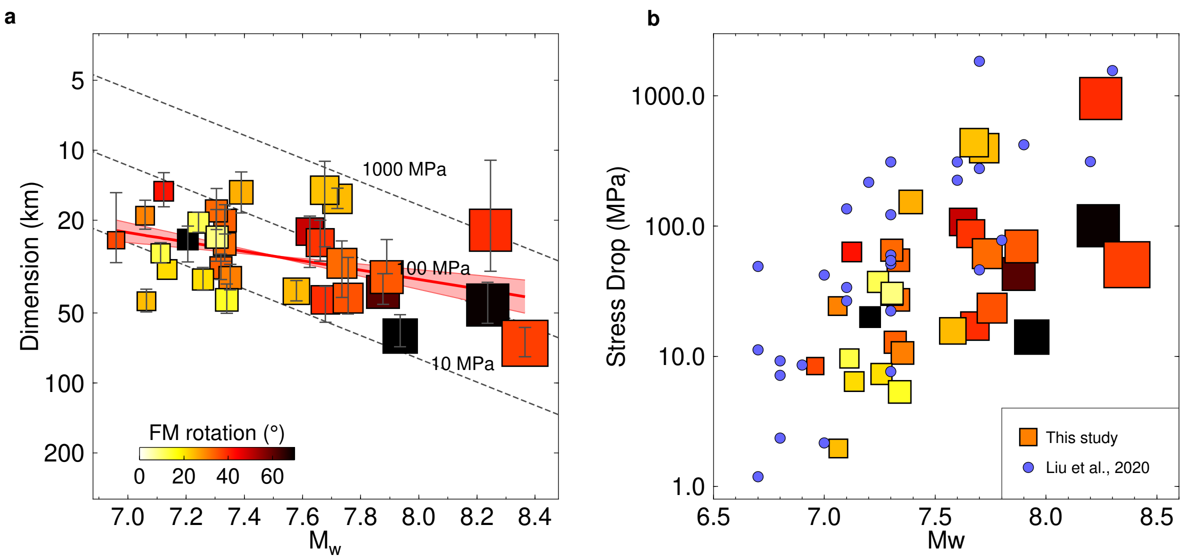

Fig. 8. Increasing stress drop with magnitude for large deep earthquakes (squares), in which size is proportional to moment magnitude. (a) Relationship between rupture dimensions and moment magnitude (Mw), shown as orange squares. Solid black lines on each square indicate the uncertainty of rupture dimensions (90% confidential interval) estimated with bootstrap re-sampling. Dashed lines represent predictions from self-similar circular rupture models. Orange line indicates a linear fit to the observed trend, with the surrounding colored area illustrating the standard deviation of the slope of this fit. The color intensity of each square reflects the 3D rotation angle of subevent focal mechanisms for each event. (b) Estimated stress drops of deep earthquakes as a function of their moment magnitude, based on a homogeneous circular rupture model. The observed trend aligns with measurements from Liu et al. (*71*) (blue circles), showing a consistent pattern of increasing stress drop with magnitude across different analyses.

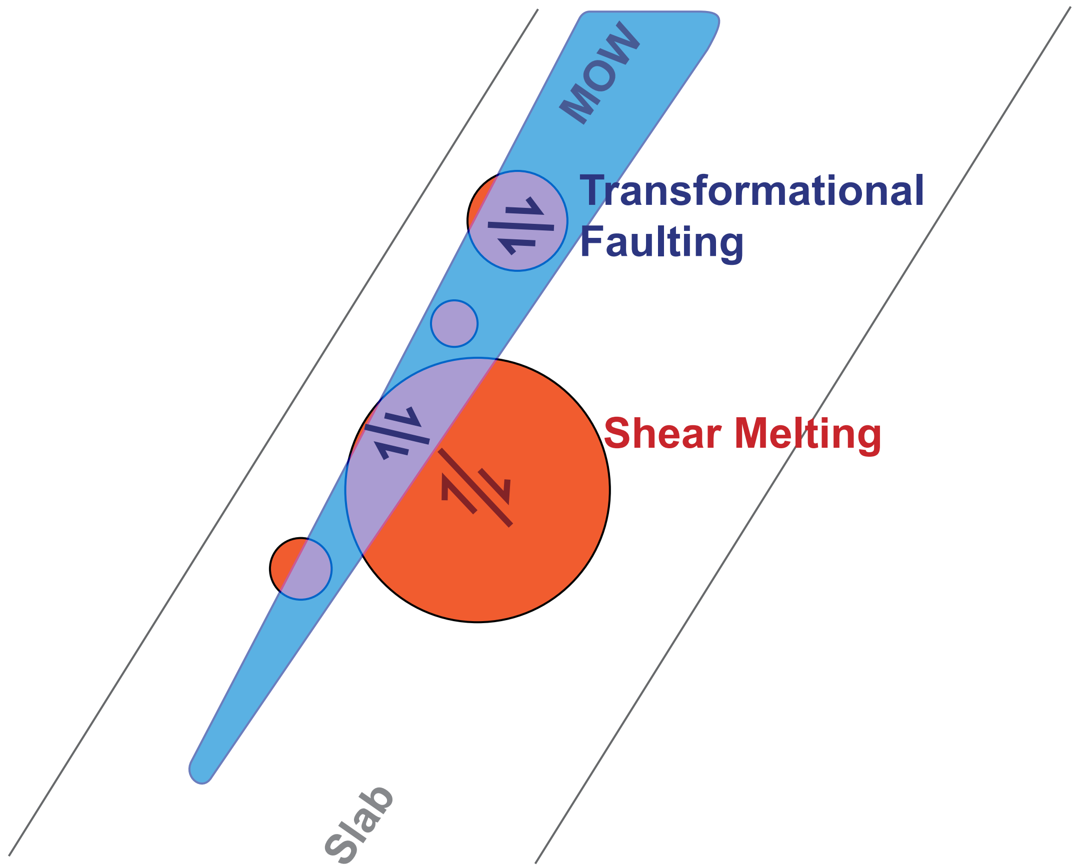

Fig. 9. Schematic representation of rupture mechanisms of deep earthquakes with different magnitudes. Smaller events are likely confined within the MOW and dominated by the transformational-faulting mechanism. Their ruptures are characterized by lower stress drop and less geometric complexity. In contrast, larger earthquakes often rupture across the MOW boundary and transition to the shear melting mechanism with large slip and moment release outside the MOW. Consequently, they have characteristics of higher stress drop and greater geometric complexity.